Model-free approach for regional ionospheric multi-instrument imaging

J. Norberg [1], S. Käki [1], L. Roininen [2], J. Mielich [3], I. I. Virtanen [4],

[1]Finnish Meteorological Institute, Helsinki, Finland
[2]Lappeenranta-Lahti University of Technology, Finland
[3] Leibniz Institute of Atmospheric Physics at the University of Rostock, Germany
[4]University of Oulu, Finland

Key Points:

- A Kalman filter application with Gaussian Markov random field priors enabling fast computation.
- No background model for ionospheric electron density is required.
- Validation with three-dimensional simulation model, as well as with real incoherent scatter radars and ionosonde measurements.

Corresponding author: J. Norberg, `johannes.norberg@fmi.fi`

Abstract

The article proposes a straightforward Kalman filter-based method for computationally efficient ionospheric electron density multi-instrument imaging. The approach uses direct ionospheric measurements, such as ionosondes, and general physical assumptions to estimate the uncertainty associated with the previous reconstructed time step. Therefore the method does not require any electron density model of the ionosphere as a background. The uncertainty is represented by an inverse covariance matrix constructed with Gaussian Markov random fields, allowing the problem to be solved numerically with relatively high resolution. The experiments utilise measurements from dense ground-based GNSS and low Earth orbit beacon satellite receiver networks as well as ionosondes. A synthetic simulation study and real data validation with a specific EISCAT incoherent scatter radar measurement campaign is carried out over Northern European sector. The method can be controlled using parameters with probabilistic and physically realistic interpretations that can be applied to both simulated and real-world data. The results show that the approach is feasible for near real-time regional ionospheric imaging. Especially, the method can be seen as an expansion to local profile measurements field of view, but with sufficient measurement coverage, it also provides information further away from the specific instrument.

1 Introduction

The early imaging approaches for ionospheric electron density considered two-dimensional iterative methods, first suggested by Austen et al. (1986, 1988). The problem was solved with algebraic reconstruction technique (ART) and simultaneous iterative reconstruction technique (SIRT). Ultimately the iterative methods are solvers for linear systems where the initial value and stopping criterion have regularising effect for ill-posed systems. With regularised least squares methods (Kaipio & Somersalo, 2005), the linear system can be solved with more explicitly stated regularising information, typically by constraining gradients and requiring smoothness from the reconstructed electron density (Markkanen et al., 1995; Seemala et al., 2014; Song, Hattori, Zhang, Liu, & Yoshino, 2021; C. H. Chen et al., 2016). The interpretation for the amount of regularisation is mathematical and not directly representable as a physical quantity.

Fremouw et al. (1992) introduced the use of basis functions for ionospheric imaging. The use of basis functions limits the space of possible solutions, reducing the dimensionality in model space from number of pixels or voxels to the number of basis-function coefficients. For a three-dimensional case the basis functions were introduced by Howe et al. (1998). Since that, the basis functions have been used most prominently in Multi-instrument data analysis system (MIDAS) (Mitchell & Spencer, 2003). Lower number of basis functions regularise the problem efficiently, but consequently limits the expressive power of the system.

In outline, increasing the number of basis functions to infinity gives rise to the Gaussian processes (GP) (Rasmussen & Williams, 2006). In GPs the regularisation results from a covariance function, which provides information on uncertainty and smoothness of the unknown. GPs were adopted to ionospheric imaging by Minkwitz et al. (2015).

Currently most of the ionospheric imaging methods are referred to as data assimilation. The data assimilation approaches operate in four-dimensional environment and can often be seen in Bayesian paradigm where the current existing information is updated with the incoming new measurements (Hajj et al., 2000; Rosen et al., 2001; Bust et al., 2004; Schunk et al., 2004; Scherliess et al., 2004; Angling & Cannon, 2004; Fridman et al., 2006; Song, Hattori, Zhang, & Yoshino, 2021). Many of these methods stem from the three dimensional variational method (Daley & Barker, 2000), however, when linear models and Gaussian errors are assumed for recursive solutions in time, the method is generally known as Kalman filter (Kalman, 1960). For an individual time-step the Kalman filter can be seen as a GP solution, where the evaluated set of points is given as a three-dimensional grid. Moreover, the solution reverts to form of regularised least squares solution, where the regularising condition is replaced with an inverse covariance matrix. Importantly, the covariance matrix connects the regularising effect to physical quantities. In data assimilation, an empirical or physical ionospheric model with its related uncertainty given as an error covariance matrix is used as a stabilising background model. Especially in global case, where some regions are poorly covered with measurements, the background fills in.

Unfortunately, Kalman filtering in three-dimensional domain is computationally expensive. The bottleneck is mainly in conveying the covariance information from time step to another. The size of the covariance matrix is the number of unknown parameters squared. Hence, in high-resolution cases the resulting covariance matrices cannot be computed or even stored in computer memory.

Largely due to the computational limitations, the recent development in ionospheric imaging has gone towards ensemble Kalman filtering (EnKF) and its further derivations (Evensen, 2009; Scherliess et al., 2017; Durazo et al., 2017; Elvidge & Angling, 2019). In EnKF the covariance matrix is replaced with a sample covariance matrix obtained from an ensemble of state vectors. These state-of-the-art ionospheric data assimilation approaches operate mostly in Global scale and utilise physical background models from empirical ones to complex physical models striving for ionospheric forecasting.

The use of scaled ionograms in ionospheric imaging was first suggested by Heaton et al. (1995). Chartier et al. (2012) used autoscaled ionosonde observations to set vertical basis functions in MIDAS algorithm. In Norberg et al. (2016) ionosonde measurements were used to build the background distribution for individual imaging snapshots. Modern assimilation methods can ingest scaled ionosonde data as direct measurements. Bust & Mitchell (2008) provide a comprehensive review covering most of the ionospheric imaging methods. Since that, Durazo et al. (2017) has one of the most inclusive introductions regarding the development with ensemble Kalman filtering.

The aim of this study is to build a lightweight and transparent ionospheric imaging system, with an attempt to minimise and generalise the required background information. The approach applies the Kalman filter approach similarly to Hajj et al. (2000, 2004); Angling & Cannon (2004); Angling & Khattatov (2006); Bust et al. (2004); Song, Hattori, Zhang, & Yoshino (2021), but without the use of a background electron density model. Instead, only the solved electron density is propagated for the estimation of the next time step and essentially ionosonde measurements are used to estimate the ionospheric variation between the consecutive states. If higher ionospheric dynamics are detected, the uncertainty on how well the previous solution predicts the current one is increased.

For numerical computations, the Gaussian Markov random field (GMRF) approach introduced for ionospheric imaging in Norberg et al. (2015, 2016, 2018) is applied. With GMRFs the desired covariance information can be implemented directly as a sparse inverse covariance i.e. precision matrix. The GMRF formalism suits here well as the sparse matrices with different covariance structures are quick to construct. As the other parts of the resulting linear system are sparse as well, the sparsity decreases computational demand significantly. Essentially, the GMRF approach combines the physical interpretation of a full covariance matrix with the computational efficiency of the regularised least squares methods.

When no background electron density model is in use, extensive and versatile ionospheric measurements are required. Hence, at the moment a sufficient coverage can be achieved only in regional scale. From here onwards the presented ionospheric imaging approach implemented in Fennoscandian sector is referred to as TomoScand.

This article first exhibits the utilised multi-instrument measurement models in Section 2. After displaying the traditional Kalman filter, in Section 3, the specific assumptions used in TomoScand system are introduced in Section 4. The data used in the study consists of real and simulated data sets and it is presented in detail in Section 5. The real data consists of 24 hour multi-instrument measurements provided by GNSS and LEO satellites, ionosondes and incoherent scatter radars. The simulated data set consists of identical instruments and geometries, but the actual electron density measurements are generated from a known synthetic ionosphere. The simulation provides an important validation scheme as the usually unknown electron density is known exactly. The experiments and the results are then presented in Sections 6 and 7 and further discussed in Section 8.

2 Measurement models

2.1 GNSS measurements

A dual-frequency GNSS measurement can be modelled as

$$\frac{c}{\alpha}\left(\frac{\omega_1^2\omega_2}{\omega_2^2-\omega_1^2}\right)\Delta\phi = TEC(L(t)) + \Phi_{arc} + b_{rec,code} + d_{sat,code} + \varepsilon_{\phi,sat,rec,\omega_1,\omega_2}(t), \qquad (1)$$

where c is the speed of light in vacuum, $\alpha = \frac{e^2}{2\epsilon_0 m}$, where e is the electron charge, m is the electron mass and ϵ_0 is the permittivity of free space. Parameters ω are the angular frequencies of the corresponding two signals of the satellite system, $\Delta\phi$ is the differential phase measurement, $TEC(L(t))$ is the slant total electron content (TEC) along the signal path $L(t)$ at time t, Φ_{arc} is the carrier phase offset, i.e. the number of undetected full cycles when the signal phase is locked for the first time and thus the same only within each continuous measurement arc. Variables b and d are differential code biases (DCB). Variable ε is the measurement error.

The slant total electron content can be modelled as an integral of electron density Ne and further approximated as a Riemann sum. Individual measurement m_j, where index j is a shorthand for specific combination of $sat, rec, code, \omega_1, \omega_2$ and t can then be written as

$$m_j = \int_{L_j} Ne(z)\mathrm{d}z + \Phi_{arc} + b_{rec,code} + d_{sat,code} + \varepsilon_j \approx \sum_{i=1}^{M_j} a_{ij}Ne_i + \Phi_{arc} + b_{rec,code} + d_{sat,code} + \varepsilon_j, \qquad (2)$$

where $a_{ij} \in \mathbb{R}$ gives the cross section length between the path L_j and voxel i, Ne_i is the electron density in voxel i and ε_j the measurement error. The DCBs are given separately for receivers and transmitters and are specific for each code combination (Håkansson et al., 2017). Within the timescales of ionospheric tomography, the DCBs are relatively stable (Mannucci et al., 1999) and are assumed independent of time and measurement geometry. Hence, for GPS and GALILEO the DCBs are shared with measurements using the same instrument and GNSS code combination. The GLONASS system uses 12 channels to switch among its operational satellites (Tamazin et al., 2018) and the DCBs are further different for each of the channels. Rigorous indexing of biases is a tedious task, but the association can provide important aid even when the biases are pre-estimated as the estimates involve uncertainties. The carrier phase offset can be estimated by levelling the precise but relative differential phase measurement with more noisy, but absolute differential code measurement (Klobuchar, 1996; Horvath & Crozier, 2007). Due to high noise level in code measurements the estimation is prone to levelling errors and affected by cycle slips.

Due to altitude of GNSS satellites, besides the ionosphere, also the plasmasphere contributes to the STEC measurement (Yizengaw & Moldwin, 2005). If the computational domain is not extended up to satellite altitudes, plasmasphere can be taken into account e.g. by dividing the integral in (2) at plasmapause and estimating the plasmaspheric contribution as an additional unknown or using plasmasphere models to set its value.

For a vector of measurements, the model can be written in matrix form as

$$\mathbf{m}_{\mathrm{GNSS}} = \mathbf{H}_{\mathrm{GNSS}}\mathbf{x} + \mathbf{B}\mathbf{b} + \mathbf{D}\mathbf{d} + \boldsymbol{\varepsilon}_{\mathrm{GNSS}}, \tag{3}$$

where matrix $\mathbf{H}_{\mathrm{GNSS}}$ consists of weigths a_{ij}, vector $\mathbf{x} = (Ne_1, \ldots, Ne_N)^{\mathrm{T}}$ and the design matrices $\mathbf{B}$ and $\mathbf{D}$ pick the correct biases for each measurement from vectors $\mathbf{b}$ and $\mathbf{d}$.

2.2 Low Earth orbit beacon satellite measurements

The low Earth orbit (LEO) dual-frequency beacon satellite systems typically use only the phase measurement (Vierinen et al., 2014). In comparison to above GNSS measurements the unknown phase offset is the dominating bias source and it is specific to each receiver for each individual continuous measurement arc. Hence, all the hardware biases can be included in phase offset. This result in a model

$$\mathbf{m}_{\mathrm{LEO}} = \mathbf{H}_{\mathrm{LEO}}\mathbf{x} + \mathbf{G}\boldsymbol{\Phi}_{arc} + \boldsymbol{\varepsilon}_{\mathrm{LEO}}. \tag{4}$$

Here matrix $\mathbf{H}_{\mathrm{LEO}}$ consists of weights a_{ij} and design matrix $\mathbf{G}$ picks the correct phase offset for each measurement from the vector $\boldsymbol{\Phi}_{arc}$. The LEO measurement is relative as the phase offset is usually solved within the analysis.

2.3 Multi-instrument measurement model

The above measurement models can be combined into a stacked matrix model

$$\mathbf{m} = \mathbf{H}\mathbf{x} + \mathbf{r}, \tag{5}$$

where

$$\begin{aligned}
\mathbf{m} &:= (\mathbf{m}_{\mathrm{GNSS}}^{\mathrm{T}}, \mathbf{m}_{\mathrm{LEO}}^{\mathrm{T}})^{\mathrm{T}}, \\
\mathbf{H} &:= \begin{bmatrix} \mathbf{H}_{\mathrm{GNSS}} & \mathbf{B} & \mathbf{D} & \mathbf{0} \\ \mathbf{H}_{\mathrm{LEO}} & \mathbf{0} & \mathbf{0} & \mathbf{G} \end{bmatrix}, \\
\mathbf{x} &:= (Ne_1^{\mathrm{T}}, \ldots, Ne_N^{\mathrm{T}}, \mathbf{b}^{\mathrm{T}}, \mathbf{d}^{\mathrm{T}}, \boldsymbol{\Phi}_{\mathrm{offset}}^{\mathrm{T}})^{\mathrm{T}}
\end{aligned}$$

and

$$\mathbf{r} := (\boldsymbol{\varepsilon}_{\mathrm{GNSS}}^{\mathrm{T}}, \boldsymbol{\varepsilon}_{\mathrm{LEO}}^{\mathrm{T}})^{\mathrm{T}} + \boldsymbol{\varepsilon}_{\mathrm{model}}. \tag{6}$$

Other measurements such as ionosonde and incoherent scatter radar measurements could be added similarly.

If the original data contain measurement error estimates, they can be fed into the tomography as such. Often ionospheric measurements are provided in higher spatio-temporal resolution than is reasonable for tomographic analysis. If the measurements are averaged to a lower spatiotemporal resolution, the error distribution can be estimated at the same time.

The model in Equation (5) is not only contaminated with measurement errors, but also with modelling, discretization or representation error $\boldsymbol{\varepsilon}_{\mathrm{model}}$. A significant source of the modelling error is in the discrete and relatively coarse spatio-temporal model that is used to capture a phenomenon that is practically continuous yet it can comprise drastic small-scale variations in both spatial and temporal dimensions the model cannot represent. The balancing of different errors in ionospheric tomography is a delicate task and if loose tuning parameters without strict physical connection and interpretation are included in the model, the modelling error is typically tuned more or less unknowingly during the general model calibration. The symptoms for insufficient compensation for modeling errors are typically non realistic high-frequency artefacts in the reconstruction. Estimating the variance and averaging in preprocessing can help covering for the modelling error, although additional relaxation is still often required. Within the field of ionospheric imaging a more profound discussion about modelling error is provided in Hajj et al. (2000), where a standard deviation of 2 TECU is assumed. Following enhanced error model, presented in Kaipio & Somersalo (2007), it is here assumed that the modelling error $\boldsymbol{\varepsilon}_{\text{model}}$ is non-zero but independent of unknown $\mathbf{x}$ and has a diagonal covariance matrix.

3 Kalman filter

The measurement model in Kalman filter can be written with Equation (5)

$$\mathbf{m}_k = \mathbf{H}_k \mathbf{x}_k + \boldsymbol{r}_k, \tag{7}$$

with the addition of subscript k denoting the time step, $\mathbf{m}_k \in \mathbf{R}^m$ is a measurement vector, matrix $\mathbf{H}_k \in \mathbb{R}^{m\times n}$ a measurement model, $\mathbf{x}_k \in \mathbb{R}^n$ is the unknown state vector and $\boldsymbol{r}_k \in \mathbb{R}^m$ a measurement error vector with normal distribution $\boldsymbol{r}_k \sim \mathcal{N}(\mathbf{0}, \mathbf{R}_k)$. The dynamic model is written as

$$\mathbf{x}_k = \mathbf{A}_{k-1}\mathbf{x}_{k-1} + \mathbf{q}_{k-1}, \tag{8}$$

where $\mathbf{A}_{k-1} \in \mathbf{R}^{n\times n}$ is a transition matrix, $\mathbf{q}_{k-1} \in \mathbf{R}^n$ is process noise with normal distribution $\mathbf{q}_k \sim \mathcal{N}(\mathbf{0}, \mathbf{Q}_k)$.

Assuming analysis results for time step $k-1$, the distribution for the predicted state at time k is

$$p(\mathbf{x}_k|\mathbf{m}_{k-1}) = \mathcal{N}(\hat{\mathbf{x}}_k, \hat{\mathbf{P}}_k), \tag{9}$$

where

$$\begin{aligned} \hat{\mathbf{x}}_k &= \mathbf{A}_{k-1}\bar{\mathbf{x}}_{k-1} \\ \hat{\mathbf{P}}_k &= \mathbf{A}_{k-1}\bar{\mathbf{P}}_{k-1}\mathbf{A}_{k-1}^{\mathrm{T}} + \mathbf{Q}_{k-1}. \end{aligned} \tag{10}$$

When the distribution for the predicted state is used as the prior distribution for the following time step k, this results in posterior distribution

$$p(\mathbf{x}_k|\mathbf{m}_k) = \mathcal{N}(\bar{\mathbf{x}}_k, \bar{\mathbf{P}}_k), \tag{11}$$

where

$$\begin{aligned} \bar{\mathbf{x}}_k &= \hat{\mathbf{x}}_k + \hat{\mathbf{P}}_k\mathbf{H}_k^{\mathrm{T}}\left(\mathbf{H}_k\hat{\mathbf{P}}_k\mathbf{H}_k^{\mathrm{T}} + \mathbf{R}_k\right)^{-1}[\mathbf{m}_k - \mathbf{H}_k\hat{\mathbf{x}}_k] \\ \bar{\mathbf{P}}_k &= \hat{\mathbf{P}}_k - \hat{\mathbf{P}}_k\mathbf{H}_k^{\mathrm{T}}\left(\mathbf{H}_k\hat{\mathbf{P}}_k\mathbf{H}_k^{\mathrm{T}} + \mathbf{R}_k\right)^{-1}\mathbf{H}_k\hat{\mathbf{P}}_k \end{aligned} \tag{12}$$

or equivalently

$$\begin{aligned} \bar{\mathbf{x}}_k &= \bar{\mathbf{P}}_k\left(\mathbf{H}_k^{\mathrm{T}}\mathbf{R}_k^{-1}\mathbf{m}_k + \bar{\mathbf{P}}_k^{-1}\hat{\mathbf{x}}_k\right) \\ \bar{\mathbf{P}}_k &= \left(\mathbf{H}_k^{\mathrm{T}}\mathbf{R}_k^{-1}\mathbf{H}_k + \hat{\mathbf{P}}_k^{-1}\right)^{-1}. \end{aligned} \tag{13}$$

4 TomoScand approach

The practical computational problems in Kalman filtering arise mostly from dealing with the $n \times n$ dimensional posterior covariance matrix $\mathbf{P_k}$ from Equation (12) or (13). Posterior covariance conveys information on the uncertainty and correlations related to the past. However, from Equation (10) it is easy to foresee a situation where the overall uncertainty is dominated by covariance $\mathbf{Q}_{k-1}$ related to ionospheric electron density dynamics between the consecutive time steps.

The TomoScand ionospheric imaging approach uses simplified Kalman filter where the predictive model (10) is given as

$$\hat{\mathbf{x}}_k = \gamma_{k-1}\bar{\mathbf{x}}_{k-1}, \tag{14}$$

$$\hat{\mathbf{P}}_k \approx \mathbf{Q}_{k-1}. \tag{15}$$

where γ is a scalar coefficient and by the above justification the covariance of the predictive distribution is approximated with $\mathbf{Q}_{k-1}$ based on local direct measurements.

The predictive covariance is defined with covariance function. In TomoScand, a Gaussian covariance function was selected with adjustable correlation lengths in three geographical coordinate directions. The standard deviation is given via an altitude dependent exponential profile

$$\sigma(z)_k = \begin{cases} \sigma_{m,k} \exp(-(z - z_{m,k})/H_{top}), & z \geq z_{m,k} \\ \sigma_{m,k} \exp((z - z_{m,k})/H_{bottom}), & z_{m,k} > z > 0, \end{cases} \tag{16}$$

where subscript k is the analysis time step, z is the altitude (m), z_m is the current peak altitude, σ_m is the peak standard deviation and H is the scale height given separately for top and bottom profiles.

4.1 Gaussian Markov random field precision

Following the three-dimensional Gaussian Markov random field approach presented in (Norberg et al., 2018), the predictive covariance structure for each step is given with a covariance function defined with standard deviation profile, correlation lengths and shape parameters, but implemented directly as a precision matrix

$$\mathbf{Q}_{k-1}^{-1} = \mathbf{L}_{k-1}^{\mathrm{T}}\mathbf{L}_{k-1}, \tag{17}$$

where $\mathbf{L}_{k-1}$ can be constructed as a combination of sparse differential matrices. The model space solution (13) can then be written as

$$\bar{\mathbf{x}}_k = \left(\mathbf{H}_k^{\mathrm{T}}\mathbf{R}_k^{-1}\mathbf{H}_k + \mathbf{L}_{k-1}^{\mathrm{T}}\mathbf{L}_{k-1}\right)^{-1}\left(\mathbf{H}_k^{\mathrm{T}}\mathbf{R}_k^{-1}\mathbf{m}_k + \mathbf{L}_{k-1}^{\mathrm{T}}\mathbf{L}_{k-1}\hat{\mathbf{x}}_k\right). \tag{18}$$

As the measurement model matrix $\mathbf{H}_k$ is sparse due to the measurement geometry and the error covariance matrix $\mathbf{R}_k$ is typically assumed diagonal, the resulting linear system (18) remains sparse. Hence, specialized solvers for sparse linear systems, such as MUMPS (Amestoy et al., 2001) can be utilised, reducing the computational cost. The GMRF approach is also discretisation invariant (Roininen et al., 2013) i.e. practically the same information can be provided for different grid sizes and resolutions.

5 Data

5.1 Real data

Geotrim, Swepos, IGS, EUREF, and FINNREF networks were used to acquire GNSS data, totaling 710 receivers measuring 31 GPS, 22 GLONASS, and 18 GALILEO satellites. The DCB's related to GNSS satellite transmitter hardware were removed from the measurements (Li et al., 2012; Wang et al., 2016). The 14 ground-based LEO receivers measured 16 overflights from CASSIOPE/e-POP (Siefring et al., 2015) and two Russian COSMOS satellites. Ionosondes measurements from Dynasonde in Tromsø, Norway, (69.6°N, 19.3°E) with two minute time resolution and Digisonde in Juliusruh, Germany (54.6°N, 13.4°E) with 5 minute time resolution are available for the most parts of the day. The data from Tromsø is scaled automatically with NeXtYZ (Zabotin et al., 2006). The Juliusruh ionograms are scaled manually; the profile calculation for the bottom side up to the F peak height is done by the NHPC true height inversion software (Reinisch & Huang, 1983; C. F. Chen et al., 1994). With both ionosondes the top side, which can not be reached by the ionosonde, is represented by a Chapman-type profile. All the ground-based instrument locations are presented in Figure 1.

To obtain validation data, a specific measurement campaign with incoherent scatter radars (ISR) of the European Incoherent Scatter Scientific Association (EISCAT) was carried out on 2018.11.09 from 00:00 to 24:00 UTC. In Tromsø, Norway (69.6°N, 19.3°E), the ultra-high frequency (UHF) radar's elevation was set to 35° and azimuth to 145°. The very-high frequency (VHF) radar, pointed to zenith, was measuring from 18:00 to 24:00 UTC. In Longyearbyen, Norway (78.2°N, 16.1°E), the EISCAT Svalbard radar's 32 m dish (ESR32) was set to 35° elevation and 150° azimuth. Both radar beams are projected in Figure 1.

5.2 Simulated data

Ionosondes and, in particular, incoherent scatter radars give high-quality ionospheric validation data, but only locally. To further understand the underlying performance and constraints of ionospheric imaging over the whole domain, a simulation study is conducted. The idea here is to create a simple synthetic ionosphere and use the instrument locations and measurement models reported in the previous sections to simulate the measurements. It is important that the model used for simulations is not used as a background or as any other input in the analysis. As here no background model is used, any ionospheric model such as International Reference Ionosphere (IRI) (Bilitza, 2018) could be utilised for simulations. However, when a function-based simulation model is chosen, measurements can be integrated with arbitrary numerical resolution. This provides a truthful approach because reconstruction at a much lower resolution naturally introduces modeling errors (Kaipio & Somersalo, 2007) and avoid so called inverse crime (Kaipio & Somersalo, 2005).

The synthetic model is constructed here with Chapman (1931) profiles

$$N(z,\chi) = N_0 \exp\left[\frac{1}{2}\left(1 - \left(\frac{z-z_0}{H}\right) - \sec(\chi)\exp\left(\frac{z-z_0}{H}\right)\right)\right], \tag{19}$$

where H is the scale height and z is the altitude. N has a maximum value $N_m = N_0(\cos(\chi)^{\frac{1}{2}})$ at the altitude $z_m = z_0 + H \log \sec(\chi)$ and parameters N_0 and z_0 can be used to control the profile accordingly. Solar zenith angle χ is given as

$$\cos(\chi(\lambda,\theta,h,\delta)) = \sin(\lambda)\sin(\delta) + \cos(\lambda)\cos(\delta)\cos(\theta+h), \tag{20}$$

where λ is the latitude, θ the longitude, h the hour angle, δ the declination of the sun.

Separate Chapman profiles for F (200–400 km) and E (90–150 km) regions are combined to form a typical ionospheric structure. The N_m parameter was set to 5×10^{11} for the F region and 0.5×10^{11} for the E region. For F region, the scale height H was set to 35 km, for day-time E region 20 km and for night 10 km. To add detail to the model a northwards decreasing altitude trend is added to profiles. At local noon the F-region peak altitude is 250 km at 40° latitude and 200 km at 75° latitude. At the same time, the day time E-region altitude is 140 km at 40° latitude and 120 km at 75° latitude.

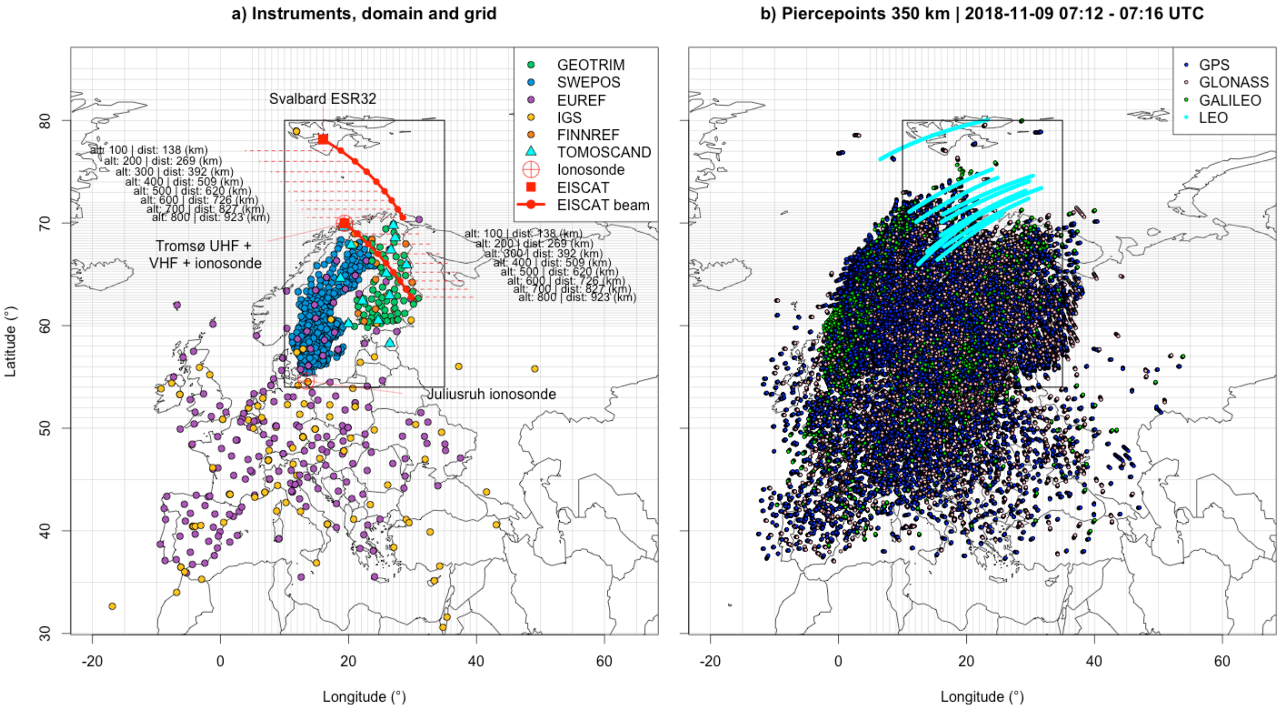

Figure 1. The geographical domain in Northern Europe. In panel a) the GNSS receiver, LEO beacon receiver, ionosonde and ISR locations used in the study are shown. EISCAT UHF and ESR32 incoherent scatter radar beams are projected. The numbers beside the radar beams give the altitudes at the corresponding locations and the great circle distances from the projection point to the instrument. The irregular latitude-longitude grid can be seen as faint gray lines in both panels a) and b). In panel b) the satellite pierce points produced by available ground receivers over an example four-minute period are given. The presented time interval has been chosen to include a low Earth orbiting (LEO) satellite overflight. The imaging analysis is carried out in a three-dimensional volume over the complete domain. The final results are visualised in the area given with the black rectangle in the middle of the domain

An ionospheric trough with a width around two degrees in latitudinal direction starts around 10 UTC and drifts from 65° to 60° latitude and disappears along the F region at dusk. Starting from 16 UTC a night-time E region is added as an auroral oval. It is built with a Chapman profile peaking at altitude of 115 km. It is centred around the peak latitude that drifts from 75° to 63°N and back.

The simulated satellite measurements are then integrated numerically. Here an integration resolution of 1 km is used. To take into account plasmaspheric contribution (Yizengaw & Moldwin, 2005), below the latitude of 54°, a uniform plasmasphere is assumed, where at zenith, the contribution up to GPS satellite altitude is 2 TECU. Measurement errors, with standard deviation $0.01/(\sin(elevation))^3$ TECU are then generated and added to measurements. At zenith this results in error of 0.01 and with elevation of 10° the error is 1.9 TECU. Besides the measurement errors, two DCB sets with standard deviations of 1 and 50 TECU were simulated.

Ionosonde and ISR profile measurements are evaluated directly at the location of the original observation. In all, this results in a simulated data set with instrument locations and measurement geometry identical to those of the real measurement

6 Experiments

On 2018.11.09 Earth's ionosphere was influenced by a co-rotating interaction region ahead of a high speed solar wind stream coming from a coronal hole. This led to slightly disturbed ionospheric conditions mainly during the night time hours between 18:00 and 21 UTC, the Kp index reached 4 -, rising to 4 between 21 and 24 UTC. The SuperMAG AE (SME) index (Newell & Gjerloev, 2011; Gjerloev, 2012) was mostly sustained at levels over 500 nT between 18:00 - 21:40 UTC with the highest peak reaching over 1000 nT at 18:42 UTC and several smaller peaks reaching over 700 nT. From 21:40 UTC onward the SME index was mostly declining.

TomoScand imaging analysis is carried out from 07:00 to 24:00 UTC. To assure availability of Tromsø ionosonde profiles for most analysis steps, a time resolution of four minutes was selected. An irregular grid is used for the analysis with larger voxel sizes at the boundary regions. The default grid is given for the different coordinate directions as follows. Latitudinal axis has 5 regions limited by parallels $30°, 50°, 60°, 72°, 85°$ and 90°N, where the intervals are divided with step sizes of 5°, 1°, 0.25°, 1° and 5° correspondingly. Longitudinal axis has 3 regions limited by meridians -20°, 5°, 40° and 65°E, divided with step sizes of 5°, 1° and 5°. The horizontal grid is plotted as gray lines in Figure 1. Altitudinal axis has 4 regions limited by heights 0, 50, 400, 600 and 1300 km, where the intervals are divided with step sizes of 25, 20, 50 and 100 km correspondingly. This result in 102600 voxels for the unknown electron density values. With bias parameters, the total number of unknowns in an individual analysis is little under 1.1×10^5. The resolution was selected so that the analysis could be run comfortably with a modern laptop.

Throughout the analysis, the parameters $N_{m,\mathrm{F}}$ and $N_{m,\mathrm{E}}$ for F and E region peak electron densities ($1/m^3$) and h_F and h_E for the corresponding altitudes (km) are adjusted using the Tromsø ionosonde. For h_F the altitude changes are limited to maximum of 5 km. For $N_{m,\mathrm{F}}$ the increase in electron density is limited to 0.5×10^{11} and the decrease to 10% between the four minute time steps. If no F-region peak is found at the time, default values of 300 km of altitude and 0.1×10^{11} electron density are given. The F-region scale height parameters in Equation (16) were set to $H_{top} = 120$ km and $H_{bottom} =$ 50 km and are fixed for the results presented here. To capture the night-time E region, the standard deviation is relaxed for the E-region altitudes at the high latitudes. A horizontally gaussian distribution is centred at the location of the Tromsø ionosonde. The width is controlled with the standard deviation parameter. Latitudinally the standard deviation is set to 6° and longitudinally to 20°. The vertical profile for the E region is given as an exponential profile (16), where the scale heights are set to $H_{top} = 60$ km and $H_{bottom} = 40$ km. The TomoScand algorithm searches for E-region peak values using ionosonde measurements from below 160 km altitude. If an E-region peak is detected, the peak electron density and its altitude are used directly for $N_{m,\mathrm{E}}$ and h_{E}. If decreased E-region peak or no peak at all is detected, the maximum damping for $N_{m,\mathrm{E}}$ between the time steps is 10%. The final prior standard deviation peak value for (16) is set as $\sigma_m = 0.1 \times N_{m,\mathrm{F}}$ for F and $\sigma_m = 0.05 \times N_{m,\mathrm{E}}$ for E region.

Before the actual analysis run, the GNSS receiver DCBs are estimated in a separate calibration run around the local midday, where all available profile measurements are used as direct measurements. Within an individual calibration run the DCBs for GPS and GALILEO receivers can typically be solved for all code combinations at once. The calibration for GLONASS DCBs can be carried out only for the channels observed at the time and the rest are estimated within the following analysis steps as they appear. Unestimated receiver DCBs are given means of 0 and standard deviations of 300 TECU. Once estimated, the receiver DCBs are given a standard deviation of 0.5 TECU for the subsequent analyses.

The analysis is started with an initial run where the ionosonde profile from Tromsø is taken as the prior mean for the entire domain. Hence, it is preferable to start the analysis at a time when the ionospheric electron density is already mainly due to solar radiation and is therefore more stable. The horizontal correlation lengths are set to 20° and the vertical to 250 km. After the initial solution, the reconstruction is updated following Equation (14), the dynamical coefficient γ_{k-1} is set to 0.9. Horizontal correlation lengths are set to 5° and vertical to 50 km. After the DCB calibration, the ionsonde and ISR profiles are not used in this study as direct measurements. Only the Tromsø ionosonde is used for adjusting the prior standard deviation as mentioned above.

7 Results

For each four minute time step a three-dimensional electron density reconstruction was analysed. With the above parameter values an individual analysis step with data processing, several plottings and saving takes around 2 min on a 16 GB, 2,7 GHz Quad-Core Intel Core i7 laptop.

7.1 Simulation data case

Analysis was started examining with clean simulated data and then adding and increasing different error sources one by one. In the trials with clean data, the reconstructions showed visible artefacts associated with higher electron density dynamics. Artifacts decreased when the error vector added to the measurements increased the estimated standard deviation. To account for modelling error the standard deviation was still increased, which further reduced the visible artefacts. Eventually, a standard deviation of 2 TECU was selected for the modelling error and added on top of estimated measurement error standard deviation. To accommodate the plasmaspheric contribution as modeling error, for measurements with 1300 km altitude piercepoints southwards from an arbitrary latitude of 55°, the modeling error is further increased as 0.5 TECU per latitude.

The addition of receiver DCBs with a standard deviation of 1 TECU, but still assuming that the measurements are unbiased, visibly worsened the reconstructions if no modelling error was added. Relaxing the prior standard deviation for the receiver DCBs or the additional modelling error standard deviation improved the situation. Finally, receiver DCBs with standard deviation of 50 TECU were added to measurements. The receiver DCBs were then estimated in a calibration run around the local midday. The mean absolute error between the solved receiver DCBs was 0.5 TECU. The analysis was then run for the whole time interval. The following results are presented for the case where the measurement errors, plasmaspheric contribution and 50 TECU DCBs are added into simulated measurements.

Simulated measurements from EISCAT UHF and ESR32 ISRs, and Juliusruh ionosonde were averaged to TomoScand's grid and compared with the corresponding profiles from the TomoScand reconstructions. In Figure 2 the simulated profiles are given in top row, the corresponding profiles from reconstructions in middle and the difference between them in the bottom row. In each panel, each column corresponds to one profile at the time indicated on the horizontal axis. With ESR32 the main structure of the modelled daytime ionosphere in Figure 2 a) can clearly be seen in the reconstructed profiles in panel b), but as indicated also by the differences in panel c), the electron density is generally slightly underestimated, especially at the bottom side. The overall correspondence along the UHF ISR profiles between Figures 2 d) and e) is clear. The differences in panel f) indicate overestimation of peak electron density and underestimation of bottom-side profile during the morning hours and during the night time activity. Comparison of the vertical profiles over Juliusruh in Figures 2 (g) and (h) show compatibility at lower latitudes, where the electron density is generally higher. A delayed change in the height of the ionosphere in the early hours causes the most visible difference between the electron densities in Figure 2 i).

In Figures 3 and 4 individual snapshots from the simulation study are presented. The top-most panel a) is an electron density section along the latitude of 23° from the ionospheric model used for the simulation and on the second row b), the corresponding slice from the three-dimensional TomoScand reconstruction is extracted. On the bottom row, first the averaged satellite pierce points at 350 km altitude within the visualised region are shown in panel c), then the integrated TEC from the ionospheric model and from the corresponding reconstruction are given in panels d) and e). Figure 3 a) shows the simulated ionosphere at 13:00 UTC / 15:00 LT. There is a clear resemblance between the model a) and the reconstruction b). However, the high-latitude decrease in electron density is faster in the reconstruction. The ionospheric trough is clearly reconstructed around the latitude of 62° and can be distinguished in both the electron density section in Figure 3 b) and the TEC map in Figure 3 e). The ionospheric pierce points at altitude of 350 km in Figure 3 c) show that the measurement coverage gets worse at the high latitudes. In Figure 4 at 20:00 UTC / 22:00 LT the comparison is performed in a situation where the night-time E region is present in the synthetic model in panel a). In the reconstruction in panel b) the electron density is vertically more concentrated and its peak value is overestimated. In TEC maps the correspondence between the model in Figure 4 d) and the reconstruction in Figure 4 e) is relatively good, but some underestimation is taking place especially at the west and east boundaries. The pierce points in Figure 6 c) show that, in addition to the high latitudes, occasionally there are fewer measurements also in the south-eastern corner of the domain.

7.2 Real data case

The real-data DCB estimation was carried out similarly to simulations with a separate calibration run. The bias calibration was validated roughly by comparing the estimated GPS DCBs to ones by MIT Haystack Observatory (Vierinen et al., 2016). The mean absolute error was 1.3 TECU.

In Figure 5 the electron density profiles from ESR32 and EISCAT UHF ISRs, and Juliusruh's ionosonde are interpolated to TomoScand's grid and combined for the time interval from 07:00 to 24:00 UTC with four minute time resolution. The top panels give the real measured profiles. In the second row the corresponding electron density profiles from TomoScand's reconstructions are given. Third row shows the IRI 2012 model default profile as another independent comparison. Fourth row gives the differences between

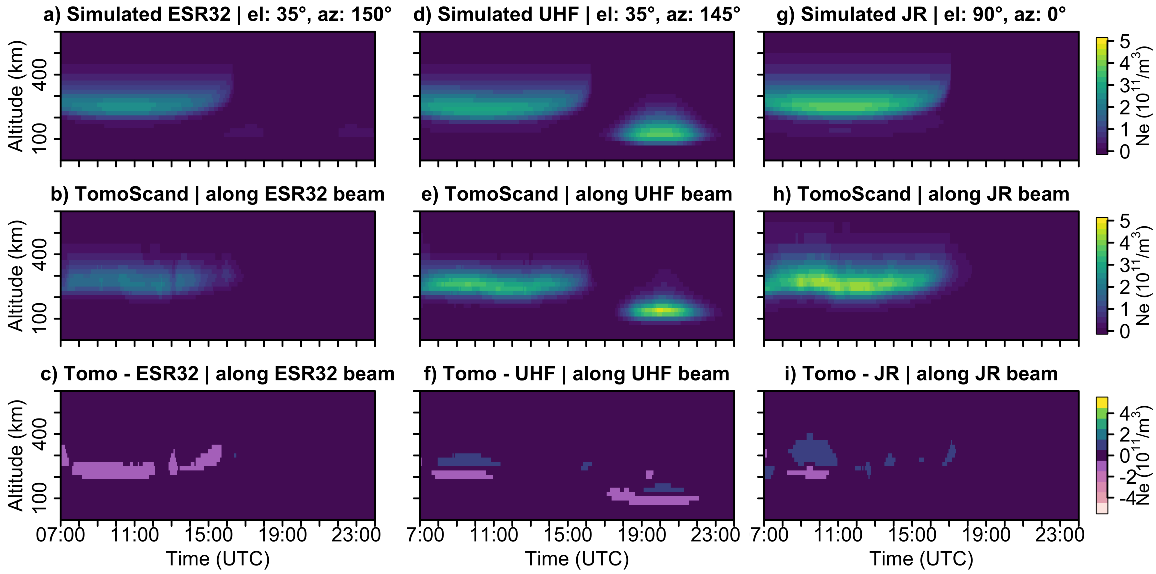

Figure 2. Comparison of validation profiles simulated from synthetic ionospheric model and corresponding profiles from TomoScand reconstruction. EISCAT ESR32 incoherent scatter radar is located in Longyearbyen, Norway (78.2°N, 16.1°E), UHF incoherent scatter radar in Tromsø, Norway (69.6°N, 19.3°E) and JR ionosonde in Juliusruh, Germany (54.6°N, 13.4°E).

the validation measurement and the corresponding TomoScand profile. On the bottom row the differences between the validation measurements and IRI 2012 model are given.

In the first column of Figure 5 the comparison is done along ESR32 ISR profile. The evolution of the morning electron density in the F region is similar between the ESR32 ISR radar measurements in panel a) and the TomoScand reconstruction in panel b). The decrease in the F region before 12:00 UTC occurs at roughly the same time. However, the radar observes relatively high electron densities starting after 12:30 UTC at E region, which then increases in altitude until 13:45 UTC, finally resulting in an enhancement in F region until 15 UTC. The TomoScand reconstruction cannot capture this evolution at lower altitudes, but suggests an increase in electron density in the F region. The differences in Figure 5 panels d) and e) are similar in shape, but slightly larger for IRI.

In Figure 5 f) the UHF ISR profiles show a normal pattern of a day-time F-region ionosphere. On the morning side, the F-region electron density increases until reaching its maximum around 11:30 UTC ($\sim 4 \times 10^{11}/m^3$), from where it starts to decrease, vanishing around 15 UTC. During the day, the F region has a horizontal wave structure indicative of travelling ionospheric disturbances. The night-time E region is first visible after 15:30, but still disappearing before 16:00. After that, the activity starting at 16:30 continues throughout the measurement period. In panel g), the TomoScand reconstruction reproduces the general features of the radar measurement. In the day-time F region, the wave structure generated by peak electron densities is replicated around the peak at 11:30 UTC. At the nigh-time E region, the resolution of detail is not as high on the TomoScand result. However, generally the night-time E-region dynamics observed by the UHF radar are well repeated in the reconstruction starting from the 15:30 onset. For F region, the differences in Figure 5 i) suggest an overestimation around the daily maximum and that the reconstruction does not capture all the wave structures present in measurements. Overestimation occurs also in the night-time E region. The IRI 2012 model in Figure 5 h) follows the day-time F-region in overall well but underestimation

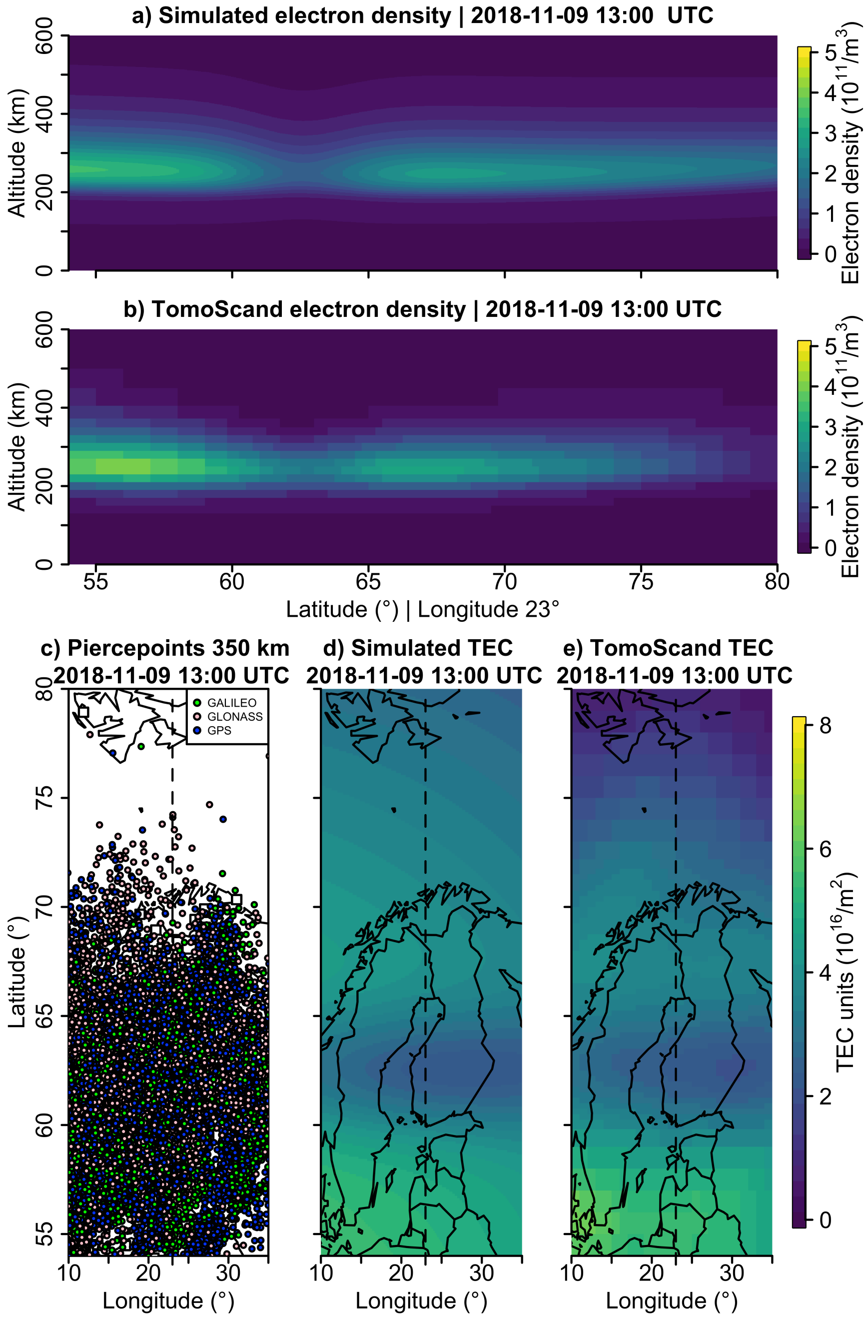

Figure 3. Comparison of synthetic ionospheric model presented in Section 5.2 and the corresponding TomoScand reconstruction at 2018-11-09 13:00 UTC. The electron density cross section from longitude 23° is given for the synthetic model in panel a) and for the TomoScand reconstruction in panel b). The ionospheric piercepoints of integrated satellite observations from the reconstruction time interval 12:56 to 13:00 UTC are shown in panel c) Simulated total electron content map is given in panel d) and the corresponding map integrated from the reconstruction in panel e).

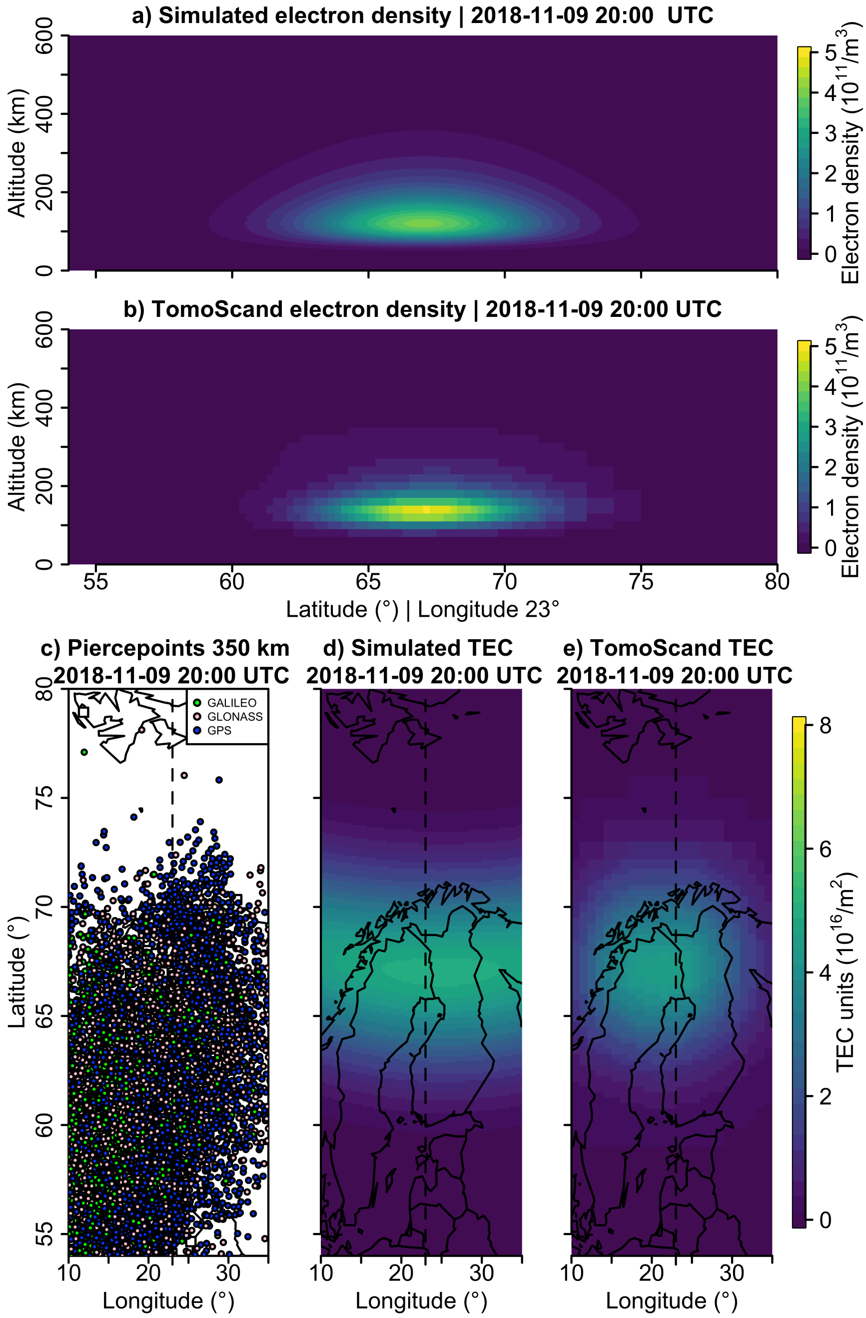

Figure 4. Comparison of synthetic ionospheric model presented in Section 5.2 and the corresponding TomoScand reconstruction at 2018-11-09 20:00 UTC. The electron density cross section from longitude 23° is given in panel a) for the synthetic model and in panel b) for the TomoScand reconstruction. The ionospheric piercepoints of integrated satellite observations from the reconstruction time interval 19:56 to 20:00 UTC are shown in panel c) Simulated total electron content map is given in panel d) and the corresponding map integrated from the reconstruction in panel e).

can be seen from the differences in Figure 5 j). The F-region wave structures and night-time E-region are not present in the standard IRI 2012 model.

At Juliusruh ionosonde location, in the third column of Figure 5, the correspondence in general diurnal variation is clear in all Real JR, TomoScand and IRI 2012 profiles. The TomoScand reconstruction in panel l) suggests an increase in F-region altitude earlier than is observed in the real data. During night time, there are differing structures between panels k) and l). The difference panel i) shows that TomoScand does not capture the day-time E layer, whereas it is included in the IRI 2012 model.

In Figures 6 and 7 two real-data reconstructions from 13:00 and 20:00 UTC are presented. The selected times are arbitrary examples from day and night-time reconstructions. In both figures the top-left panel a) presents a cross section from the reconstruction along longitude 23°, below are shown the profile measurements from c) EISCAT ESR32 and d) EISCAT UHF ISRs, and e) Juliusruh ionsonde with red lines and the corresponding profile from the TomoScand reconstruction with black line. The cyan line shows the prior electron density given for the time step and the dashed cyan lines the 95% prior probability interval. The measured and reconstructed profiles are individual columns from corresponding instruments and times from Figure 5. On right-hand side, on panel b), the TEC map is integrated from the reconstruction with the validation instrument locations and ISR beams shown once more.

Figure 6 shows the reconstruction and validations at 13:00 UTC / 15 LT. The panels a) and b) present typical northwards and eastwards decreasing evening-side trends in the electron density. In panel c), the measured ESR32 beam shows a significant E-region enhancement which is not captured in the TomoScand reconstruction. Instead, the F-region electron density is overestimated. The same mismatch was observed already in the Figure 5 between panels a) and b). Figure 6 d) shows a strong correspondence between the measured UHF ISR and TomoScand's reconstruction, with just minor overestimation in the reconstruction. In Juliusruh ionosonde profiles, in panel e), the correspondence is even more clear. The satellite pierce points, shown in Figure 5 c) correspond to this case.

Figure 7 shows the reconstruction at 20:00 UTC / 22 LT. The electron density cross section from longitude 23° shows a significant enhancement in the E region between the latitudes of 64 and 73°. This can be seen as band of enhanced electron content in the TEC map in Figure 7 b). ESR32 profiles in Figure 7 c) are somewhat on the level at the F-region altitude. The profiles in Figure 7 d) show that a similar E-region enhancement can be seen in the UHF ISR measurement. The reconstructed peak is in the middle of the two measured profiles within the four minute time interval. In Juliusruh, in Figure 7 e), the general resemblance is good with minor overestimation in electron density and underestimation in its altitude. The satellite pierce points, shown in Figure 6 c) correspond to this case.

In Table 1 the mean absolute relative errors for peak electron densities and mean absolute errors for the corresponding altitudes are given. For the peak altitudes the mean absolute errors are given as kilometres and for peak electron density (Ne), relative mean absolute errors are given as a percentage of the more accurate measurement listed second in the first column. The mean errors are given separately for the *total* time interval from 07:00 to 24:00 UTC, *Day* time from 07:00 to 15:30 UTC and *Night* time from 15:30 to 24:00 UTC. The day-night division is based on the visible change in UHF measurements visible in Figure 5. The results show that along the UHF beam TomoScand outperforms IRI 2012 at all times. Along the ESR32 beam, TomoScand's performance is also better than IRI's, but the difference is not quite as significant. Above Juliusruh, the TomoScand results for the electron density peak are better than the IRI model, but for the daily peak height the IRI model is slightly more accurate. In the eighth row, the TomoScand reconstruction is compared with VHF ISR measurements, which were only available from 18-24 UTC. On the row second to last, the Tromsø ionosonde measurement is compared to VHF ISR measurement. TomoScand match the VHF ISR measurements better than those provided by ionosonde at the same location. On the last row, the Tromsø ionosonde measurement is compared to the low-elevation UHF ISR measurement.

Mean error in peak value	Ne [total]	Ne [Day]	Ne [Night]	Alt [total]	Alt [Day]	Alt [Night]
TomoScand vs. UHF ISR	31 %	13 %	49 %	22 km	16 km	29 km
IRI 2021 vs. UHF ISR	53 %	27 %	79 %	91 km	24 km	157 km
TomoScand vs. ESR32 ISR	47 %	49 %	45 %	35 km	34 km	15 km
IRI 2012 vs. ESR32 ISR	54 %	52 %	56 %	53 km	54 km	53 km
TomoScand vs. Juliusruh IS	22 %	12 %	33 %	23 km	33 km	13 km
IRI 2012 vs. Juliusruh IS	37 %	26 %	47 %	20 km	13 km	26 km
TomoScand vs. VHF ISR	NA	NA	58 %	NA	NA	33 km
Tromsø ionosonde vs. VHF ISR	NA	NA	88 %	NA	NA	40 km
Tromsø ionosonde vs. UHF ISR	51 %	24 %	80 %	42 km	32 km	51 km

Table 1. Mean absolute relative errors for electron density (Ne) and mean absolute errors for peak altitude between TomoScand reconstructions, EISCAT incoherent scatter radars (ISR), ionosondes (IS) and International Reference Ionosphere (IRI) 2012 model.

8 Discussion

The calibration of the covariance parameters, preceding the results presented in the previous chapter, confirmed the well-known fact that the information on the ionospheric height profile from ground-based satellite measurements is very limited. With large scale heights for the standard deviation profile, the reconstruction would spread over a too wide range of altitudes. Thus, the electron density uncertainty must be concentrated in a relatively narrow region, in this case near the peak electron density heights observed by the Tromsø ionosonde.

The simulation results show that the TomoScand approach works generally as anticipated and changes in the various parameters cause physically realistic responses in the results. The method can be used consistently in both simulation and real data cases with the same set of parameters throughout the analysis interval. Importantly, the results in Table 1 suggest that the electron density maximum and its height along the UHF beam can be reconstructed with better precision than is given by extrapolating the ionosonde's electron density measurement to the same location or by using the default IRI 2012 model. Significantly this holds also for the night-time E region, where the reconstructed TomoScand profiles correspond to VHF profiles better than ionosonde at the same location. At lower latitudes, in Juliusruh, TomoScand's performance is generally more or less on a par with the UHF comparison. As the IRI 2012 model performs better at lower latitudes, the difference between TomoScand and the model is less significant.

The underestimation of high-latitude electron content results from regionally poor measurement coverage combined with the damping effect of the prediction step's γ_{k-1} parameter. In simulations the underestimation is clear at ESR32 in Figure 2 b) located

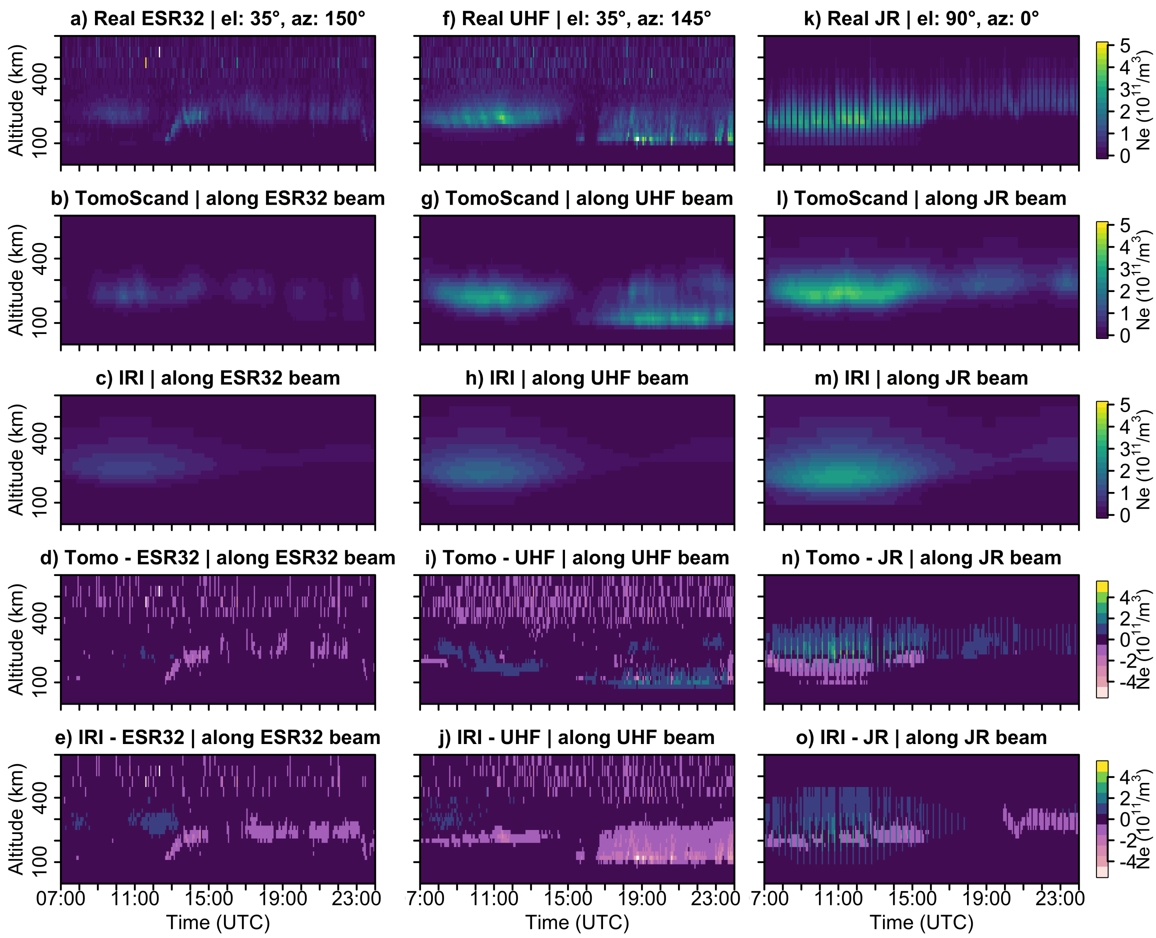

Figure 5. Comparison of measured real validation profiles, corresponding profiles from TomoScand reconstruction and IRI 2012 model from 2018.11.09. EISCAT ESR32 incoherent scatter radar is located in Longyearbyen, Norway (78.2°N, 16.1°E), UHF incoherent scatter radar in Tromsø, Norway (69.6°N, 19.3°E) and JR ionosonde in Juliusruh, Germany (54.6°N, 13.4°E).

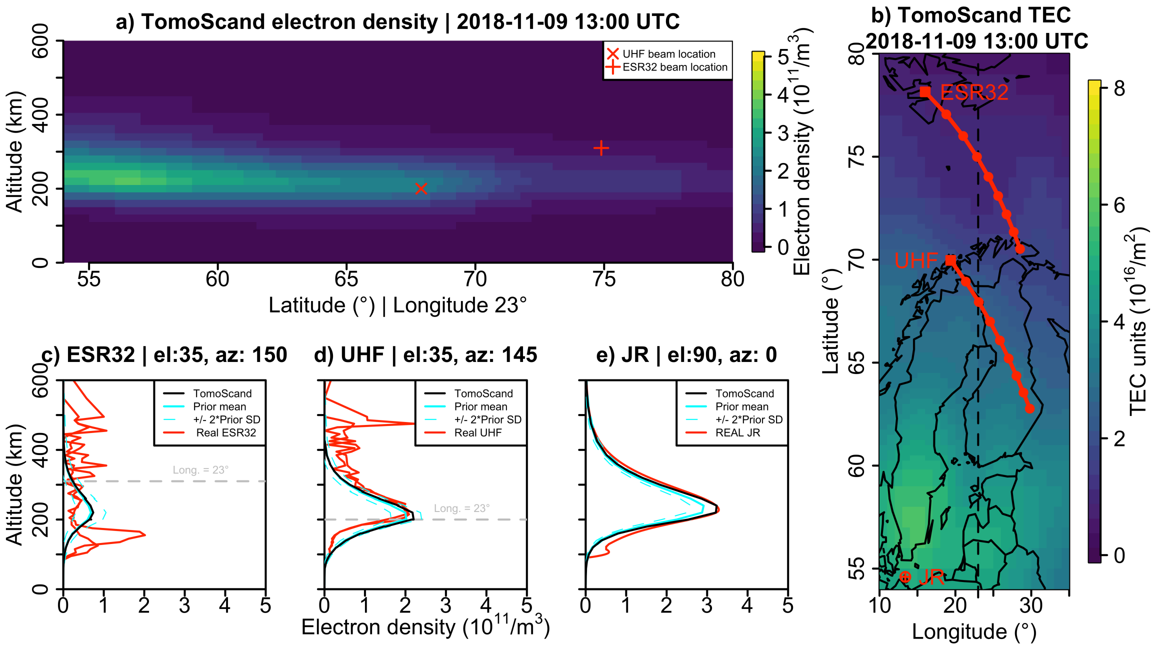

Figure 6. TomoScand reconstruction of ionospheric electron density from the measurements collected from 2018-11-09 12:56 to 13:00 UTC and profile validations. The electron density cross section from longitude 23° is given in panel a) and the corresponding TEC map integrated from the reconstruction in panel b). In panels c), d), and e) the measured EISCAT ESR32 and UHF incoherent scatter radar and Juliusruh ionosonde profiles are given in red, the related reconstruction profiles with black and the prior distribution with cyan lines.

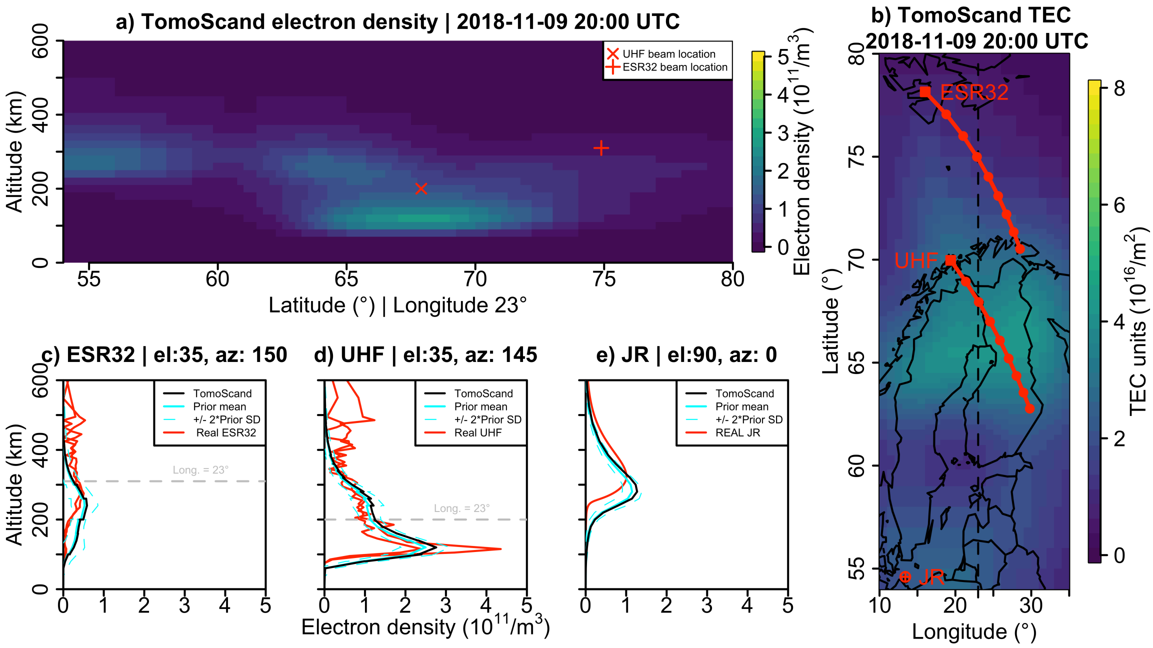

Figure 7. TomoScand reconstruction of ionospheric electron density from the measurements collected from 2018-11-09 19:56 to 20:00 UTC and profile validations. The electron density cross section from longitude 23° is given in panel a) and the corresponding TEC map integrated from the reconstruction in panel b). In panels c), d), and e) the measured EISCAT ESR32 and UHF incoherent scatter radar and Juliusruh ionosonde profiles are given in red, the related reconstruction profiles with black and the prior distribution with cyan lines.

at highest latitudes. Results with real data, in Figure 5 b), indicates also underestimation at evening and night time. A visual comparison of pierce points during the analysis run suggests that the patches with higher electron density in Figure 5 b) could be associated with periods of better measurement coverage at higher latitudes. How the underestimation at high latitudes shows up in in individual reconstructions can be seen most clearly in the cross section and TEC map comparisons in Figure 3. The situation could be improved by increasing the horizontal correlation lengths, but this could also reduce the detail of the reconstructions in areas where more comprehensive measurements are available.

Problems in reconstructing the enhanced E-region electron density measured with ESR32 ISR around 13 UTC can be traced by comparing the pierce points at the time in Figure 3 c) with ESR32 beam projection in Figure 1 a). Especially at the location where ESR32 beam propagates in E-region altitudes the satellite measurements are extremely sparse. Besides the sparsity of the measurements, as Tromsø ionosonde is not observing any E-region activity, the predictive standard deviation is kept low at the corresponding altitudes, making E-region enhancements in reconstructions unlikely.

The dynamical scaler γ_{k-1} can be seen as simple continuity equation. The approach could be improved by adjusting γ_{k-1} based e.g. on local time. However, as the idea here is to keep the approach as model-free as possible, the value is fixed. The γ_{k-1} parameter is also related to numerical stability. Due to the idiosyncratic measurement geometry and the shape of the standard deviation profiles the balancing for increased electron densities at extreme altitudes, where typically little variation is expected, is problematic. After such an event the measurements often struggle to have as strong evidence to show that these events have ceased. This results as artefacts in the reconstructions that pass from time step to another, eventually ruining the analysis run. The role of parameter $\gamma_{k-1} < 1$ is to attenuate the electron density in the whole domain. The new measurements then pull the electron density back to the real level.

In TomoScand approach the DCB calibration is best to perform during the day time with a strong and smooth ionosphere. When the DCBs are combined correctly the GPS and GALILEO measurements provide information from both the ionosphere and the biases. If bias estimation is performed on the simulated data during the ionospheric trough, the results show a trough already in the first solution. In this analysis, the once estimated biases were not updated in subsequent analysis. This has to do with the dynamical model in use. If the biases would be estimated each time, the dynamical step with $\gamma_{k-1} < 1$ would gradually push the whole ionospheric contribution to the bias estimates.

The large differences between Tromsø VHF ISR and the ionosonde measurements in Table 1 could reflect the different resolutions of the instruments and the details of the ionosphere. Although the instruments are located practically in the same place, the aperture angles as well as operating principles of the instruments are different (Lilensten et al., 2005). It should also be borne in mind that, in the case of Tromsø Dynasonde, these are the results of automated analysis. Further conclusions from the discrepancy would require a more detailed analysis, however they provide a good reminder of ionospheric high-latitude dynamics and the level of accuracy that can be expected with ionospheric measurements.

9 Conclusions

The results with both simulated and real data suggest that TomoScand approach for ionospheric imaging provides generally realistic electron density reconstructions. In the real data case the validation with UHF incoherent scatter radar demonstrates competent performance for both day and night times. Compared to the low-elevation UHF incoherent scatter radar measurement, which extends at F-band altitudes to nearly 400 km from Tromsø, the imaging results show better agreement than the extrapolation from the ionosonde. Further away, at Juliusruh ionosonde with a distance of 1700 km from Tromsø, the general diurnal behaviour is captured in the reconstructions. The comparison with ESR32 incoherent scatter radar in Longyearbyen, Svalbard, demonstrates how the results will approach zero at areas with only few measurements. Although the results may not justify the actual scientific use of the method at the latitudes of ESR32, these boundary data are important for realistic reconstructions in the more central part of the domain.

The proposed approach can be seen especially as an extension for the field of view of radar-type measurements such as ionosondes and incoherent scatter radars. The analysis can also be performed under slightly disturbed ionospheric conditions. The performance could probably be yet improved by taking into account of daily evolution in the dynamic scaling term or by using an ionospheric model to determine the F-layer prior height further away from the deployed input profile measurements. This would still differ from using the model as a background electron density in assimilation. A desirable future development would be a network of profile measurements. Profiles could be used to determine the non-uniform prior standard deviation mask, but also as direct measurements at their locations.

10 Open Research

All the input, simulation and validation data used in the study (Norberg, 2022) are available at Zenodo via 10.5281/zenodo.6760141 as one dataset with acknowledgements given below.

The ground-based GNSS measurements are provided in an hdf5 file as geometry free combinations with satellite hardware biases removed. The daily GNSS data and the precise orbits are provided by International GNSS Service (IGS) and the International Association of Geodesy Reference Frame Sub-Commission for Europe Permanent GNSS Network (EUREF EPN) available from the EUREF EPN Regional Data Centre by Bundesamt für Kartografie und Geodäsie (https://igs.bkg.bund.de/). The dense GNSS networks in Finland and Sweden are provided by Geotrim (www.geotrim.fi) and Swepos https://swepos.lantmateriet.se. The data can be used for non-commercial scientific research. Daily multi-GNSS differential code bias estimates were obtained through NASA Crustal Dynamics Data Information System (CDDIS) https://cddis.nasa.gov/archive/gnss/products/bias/.

The GUISDAP analysed EISCAT incoherent scatter radar data was accessed via Madrigal Database at EISCAT (https://madrigal.eiscat.se/madrigal/) and EISCAT Dynasonde data via Dynasonde database (https://dynserv.eiscat.uit.no/DD/login.php) with simple registration. EISCAT is an international association supported by research organisations in China (CRIRP), Finland (SA), Japan (NIPR and ISEE), Norway (NFR), Sweden (VR), and the United Kingdom (UKRI). These data are the intellectual property of the EISCAT Scientific Association. They may be freely used for the purpose of illustration for teaching and for non-commercial scientific research, provided that the source is acknowledged and to the extent justified by the non-commercial purpose to be achieved. Substantial use of these data should be discussed at an early stage with knowledgeable scientists within the EISCAT Scientific Association (EISCAT's Headquarters, enquires@eiscat.se, can provide advice on suitable contacts) in order to clarify matters of use, calibration and potential co-authorship. Any further distribution of these data, including installation in any database, must be accompanied by this statement and subject to the same conditions of use. The Juliusruh Ionosonde data is owned by the Leibniz Institute of Atmospheric Physics Kuehlungsborn.

An hdf5 file with independently solved (Vierinen et al., 2016) receiver DCBs used for comparison is included in the dataset (Norberg, 2022). The GPS data used for DCB comparison and access through the Madrigal distributed data system are provided by the Massachusetts Institute of Technology (MIT) under support from US National Science Foundation grant AGS-1242204. Data for TEC processing is provided from the following organizations: UNAVCO, Scripps Orbit and Permanent Array Center, Institut Geographique National, France, International GNSS Service, The Crustal Dynamics Data Information System (CDDIS), National Geodetic Survey, Instituto Brasileiro de Geografia e Estatística, RAMSAC CORS of Instituto Geográfico Nacional de la República Argentina, Arecibo Observatory, Low-Latitude Ionospheric Sensor Network (LISN), Topcon Positioning Systems, Inc., Canadian High Arctic Ionospheric Network, Centro di Ricerche Sismologiche, Système d'Observation du Niveau des Eaux Littorales (SONEL), RENAG : REseau NAtional GPS permanent, GeoNet - the official source of geological hazard information for New Zealand, GNSS Reference Networks, Finnish Meteorological Institute, and SWEPOS - Sweden. Access to these data is provided by madrigal network via: http://cedar.openmadrigal.org/.

Version 2.2 of the Pyglow used for obtaining IRI 2012 data is developed and available at https://github.com/timduly4/pyglow. The International Reference Ionosphere (IRI) is an international project sponsored by the Committee on Space Research (COSPAR) and the International Union of Radio Science (URSI). GPSTk is sponsored by the Space and Geophysics Laboratory, within the Applied Research Laboratories at the University of Texas at Austin (ARL:UT). Version 8.0.0 of the GPSTk used for GNSS data processing is preserved and available via https://github.com/SGL-UT/GPSTk and developed openly at https://gitlab.com/sgl-ut/gnsstk-apps.

Multifrontal Massively Parallel sparse direct Solver (MUMPS) used for matrix inversion is developed at http://mumps.enseeiht.fr. The R language MUMPS interface, RMUMPS, is developed openly at https://github.com/morispaa/rmumps. Besides the computation time, the results presented in the study do not dependent significantly on the third party software mentioned above or their specific versions, but other solvers could be used as well.

In addition to all of the data providers and software developers mentioned above, we are grateful to the SuperMAG partners and members of the CASSIOPE/e-POP science team, especially the Coherent Electromagnetic Radiation tomography experiment (CER) for low Earth orbiting beacon radio transmissions.

References

Amestoy, P. R., Duff, I. S., Koster, J., & L'Excellent, J.-Y. (2001). A Fully Asynchronous Multifrontal Solver Using Distributed Dynamic Scheduling. *SIAM Journal on Matrix Analysis and Applications*, *23*(1), 15–41. doi: 10.1137/S0895479899358194

Angling, M. J., & Cannon, P. S. (2004). Assimilation of radio occultation measurements into background ionospheric models. *Radio Science*, *39*, 1–11. doi: 10.1029/2002RS002819

Angling, M. J., & Khattatov, B. (2006). Comparative study of two assimilative models of the ionosphere. *Radio Science*, *41*(April), 1–11. doi: 10.1029/2005RS003372

Austen, J. R., Franke, S., Liu, C., & Yeh, K. C. (1986). Application of computerized tomography techniques to ionospheric research. In A. Tauriainen (Ed.), *International beacon satellite symposium on radio beacon contribution to the study of ionization and dynamics of the ionosphere and to corrections to geodesy and technical workshop, proceedings. part 1 (a87-50101 22-46).* (pp. 25–35.). Oulu, Finland: University of Oulu.

Austen, J. R., Franke, S. J., & Liu, C. H. (1988). Ionospheric imaging using computerized tomography Jeffrey. *Radio Science*, *23*(3), 299–307.

Bilitza, D. (2018). IRI the international standard for the ionosphere. *Advances in Radio Science*, *16*, 1–11. doi: 10.5194/ars-16-1-2018

Bust, G. S., Garner, T. W., & II, T. L. G. (2004). Ionospheric Data Assimilation Three-Dimensional {(IDA3D)}: A global, multisensor, electron density specification algorithm. *J. Geophys. Res.*, *109*. doi: 10.1029/2003JA010234

Bust, G. S., & Mitchell, C. N. (2008). History, current state, and future directions of ionospheric imaging. *Rev. Geophys.*, *46*. doi: 10.1029/2006RG000212

Chapman, S. (1931, sep). The absorption and dissociative or ionizing effect of monochromatic radiation in an atmosphere on a rotating earth part {I} and part {II}. Grazing incidence. *Proceedings of the Physical Society*, *43*(5), 483–501. doi: 10.1088/0959-5309/43/5/302

Chartier, A. T., Smith, N. D., Mitchell, C. N., Jackson, D. R., & Patilongo, P. J. C. (2012). The use of ionosondes in GPS ionospheric tomography at low latitudes. *J. Geophys. Res.*, *117*. doi: 10.1029/2012JA018054

Chen, C. F., Reinisch, B. W., Scali, J. L., Huang, X., Gamache, R. R., Buonsanto, M. J., & Ward, B. D. (1994). The accuracy of ionogram-derived N(h) profiles. *Advances in Space Research*, *14*(12), 43–46. doi: https://doi.org/10.1016/0273-1177(94)90236-4

Chen, C. H., Saito, A., Lin, C. H., Yamamoto, M., Suzuki, S., & Seemala, G. K. (2016). Medium-scale traveling ionospheric disturbances by three-dimensional ionospheric GPS tomography 3. Space science. *Earth, Planets and Space*, *68*(1). doi: 10.1186/s40623-016-0412-6

Daley, R., & Barker, E. (2000). *NAVDAS Source Book. NRL Atmospheric Variational Data Assimilation System.*

Durazo, J. A., Kostelich, E. J., & Mahalov, A. (2017). Local ensemble transform Kalman filter for ionospheric data assimilation: Observation influence analysis during a geomagnetic storm event. *Journal of Geophysical Research: Space Physics*, *122*(9), 9652–9669. doi: 10.1002/2017JA024274

Elvidge, S., & Angling, M. J. (2019). Using the local ensemble Transform Kalman Filter for upper atmospheric modelling. *Journal of Space Weather and Space Climate*, *9*, A30. doi: 10.1051/swsc/2019018

Evensen, G. (2009). *Data Assimilation, the Ensemble Kalman Filter* (2nd ed.). Dordrecht Heidelberg London New York: Springer-Verlag. doi: 10.1007/978-3-642-03711-5

Fremouw, E. J., Secan, J. A., & Howe, B. M. (1992). Application of stochastic inverse theory to ionospheric tomography. *Radio Science*, *27*(5), 721–732. doi: 10.1029/92RS00515

Fridman, S. V., Nickisch, L. J., Aiello, M., & Hausman, M. (2006). Real-time reconstruction of the three-dimensional ionosphere using data from a network of GPS receivers. *Radio Science*, *41*(5), 1–7. doi: 10.1029/2005RS003341

Gjerloev, J. W. (2012). The SuperMAG data processing technique. *Journal of Geophysical Research: Space Physics*, *117*(9), 1–19. doi: 10.1029/2012JA017683

Hajj, G. A., Lee, L. C., Pi, X., Romans, L. J., Schreiner, W. S., Straus, P. R., & Wang, C. (2000). COSMIC GPS ionospheric sensing and space weather. *Terrestrial, Atmospheric and Oceanic Sciences*, *11*(1), 235–272. doi: 10.3319/TAO.2000.11.1.235(COSMIC)

Hajj, G. A., Wilson, B. D., Wang, C., Pi, X., & Rosen, I. G. (2004). Data assimilation of ground GPS total electron content into a physics-based ionospheric model by use of the Kalman filter. *Radio Science*, *39*(1), 1–17. doi: 10.1029/2002rs002859

Håkansson, M., Jensen, A. B., Horemuz, M., & Hedling, G. (2017). Review of code and phase biases in multi-GNSS positioning. *GPS Solutions*, *21*(3), 849–860. doi:

10.1007/s10291-016-0572-7

Heaton, J. A. T., Pryse, S. E., & Kersley, L. (1995). Improved background representation, ionosonde input and independent verification in experimental ionospheric tomography. *Ann. Geophys.*, *13*(1297-1302), 1297–1302.

Horvath, I., & Crozier, S. (2007). Software developed for obtaining GPS-derived total electron content values. *Radio Science*, *42*(2). doi: 10.1029/2006RS003452

Howe, B. M., Runciman, K., & Secan, J. A. (1998). Tomography of the ionosphere: Four-dimensional simulations. *Radio Science*, *33*(1), 109–128. doi: 10.1029/97RS02615

Kaipio, J., & Somersalo, E. (2005). *Statistical and Computational Inverse Problems.* New York: Springer.

Kaipio, J., & Somersalo, E. (2007). Statistical inverse problems: Discretization, model reduction and inverse crimes. *Journal of Computational and Applied Mathematics*, *198*(2), 493–504. doi: 10.1016/j.cam.2005.09.027

Kalman, R. E. (1960). A new approach to linear filtering and prediction problems. *Journal of Fluids Engineering, Transactions of the ASME*, *82*(1), 35–45. doi: 10.1115/1.3662552

Klobuchar, J. A. (1996). Ionospheric effects on GPS positioning. In B. W. Parkinson & J. J. Spilker (Eds.), *Global positioning system : Theory and applications, vol. 1* (pp. 485–515). American Institute of Aeronautics and Astronautics, Inc. doi: https://doi.org/10.2514/4.866388

Li, Z., Yuan, Y., Li, H., Ou, J., & Huo, X. (2012). Two-step method for the determination of the differential code biases of COMPASS satellites. *Journal of Geodesy*, *86*(11), 1059–1076. doi: 10.1007/s00190-012-0565-4

Lilensten, J., Cander, L. R., Rietveld, M., Cannon, P. S., & Barthélémy, M. (2005). Comparison of EISCAT and ionosonde electron densities: application to a ground-based ionospheric segment of a space weather programme. *Annales Geophysicae*, *23*, 183–189.

Mannucci, A. J., Iijima, B., Sparks, L., Pi, X., Wilson, B., & Lindqwister, U. (1999). Assessment of global TEC mapping using a three-dimensional electron density model. *Journal of Atmospheric and Solar-Terrestrial Physics*, *61*(16), 1227–1236. doi: 10.1016/S1364-6826(99)00053-X

Markkanen, M., Lehtinen, M. S., Nygrén, T., Pirttilä, J., Helenius, P., Vilenius, E., … Khudukon, B. Z. (1995). Bayesian approach to satellite radiotomography with applications in the Scandinavian sector. *Ann. Geophys.*, *13*, 1277–1287.

Minkwitz, D., Van Den Boogaart, K. G., Gerzen, T., & Hoque, M. M. (2015). Tomography of the ionospheric electron density with geostatistical inversion. *Annales Geophysicae*, *33*, 1071–1079. doi: 10.5194/angeo-33-1071-2015

Mitchell, C. N., & Spencer, P. S. J. (2003). A three-dimensional time-dependent algorithm for ionospheric imaging using GPS. *Annals of Geophysics*, *46*(4), 687–696. doi: 10.4401/ag-4373

Newell, P. T., & Gjerloev, J. W. (2011). Evaluation of SuperMAG auroral electrojet indices as indicators of substorms and auroral power. *Journal of Geophysical Research: Space Physics*, *116*(12), 1–12. doi: 10.1029/2011JA016779

Norberg, J. (2022). TomoScand_dataset_2018_313 (Version 1.0.0) [Dataset]. doi: 10.5281/zenodo.6760141

Norberg, J., Roininen, L., Vierinen, J., Amm, O., McKay-Bukowski, D., & Lehtinen, M. S. (2015). Ionospheric tomography in Bayesian framework with Gaussian Markov random field priors. *Radio Science*, *50*(2), 138–152. doi: 10.1002/2014RS005431

Norberg, J., Vierinen, J., Roininen, L., Orispää, M., Kauristie, K., Rideout, W. C., … Lehtinen, M. S. (2018). Gaussian Markov Random Field Priors in Ionospheric 3-D Multi-Instrument Tomography. *IEEE Transactions on Geoscience and Remote Sensing*, 1–13. doi: 10.1109/TGRS.2018.2847026

Norberg, J., Virtanen, I. I., Roininen, L., Vierinen, J., Orispää, M., Kauristie, K., & Lehtinen, M. S. (2016). Bayesian statistical ionospheric tomography improved by incorporating ionosonde measurements. *Atmospheric Measurement Techniques*, *9*(4), 1859–1869. doi: 10.5194/amt-9-1859-2016

Rasmussen, C. E., & Williams, C. K. I. (2006). *Gaussian Processes for Machine Learning.* (T. Dietterich, C. Bishop, D. Heckerman, M. Jordan, & M. Kearns, Eds.). Cambridge: MIT Press. doi: 10.1142/S0129065704001899

Reinisch, B. W., & Huang, X. (1983). Automatic calculation of electron density profiles from digital ionograms: 3. Processing of bottomside ionograms. *Radio Science*, *18*(3), 477–492. doi: 10.1029/RS018i003p00477

Roininen, L., Piiroinen, P., & Lehtinen, M. S. (2013, may). Constructing continuous stationary covariances as limits of the second-order stochastic difference equations. *Inverse Problems and Imaging*, *7*(2), 611–647. doi: 10.3934/ipi.2013.7.611

Rosen, I. G., Wang, C., Hajj, G. A., Pi, X., & Wilson, B. (2001). An adjoint method based approach to data assimilation for a distributed parameter model for the ionosphere. *Proceedings of the IEEE Conference on Decision and Control*, *5*, 4406–4408. doi: 10.1109/CDC.2001.980895

Scherliess, L., Schunk, R. W., Gardner, L. C., Eccles, J. V., Zhu, L., & Sojka, J. J. (2017). The USU-GAIM-FP data assimilation model for ionospheric specifications and forecasts. In *2017 32nd general assembly and scientific symposium of the international union of radio science, ursi gass 2017* (Vol. 2017-Janua, pp. 1–4). doi: 10.23919/URSIGASS.2017.8104978

Scherliess, L., Schunk, R. W., Sojka, J. J., & Thompson, D. C. (2004). Development of a physics-based reduced state Kalman filter for the ionosphere. *Radio Science*, *39*(1), 1–12. doi: 10.1029/2002rs002797

Schunk, R. W., Scherliess, L., Sojka, J. J., Thompson, D. C., Anderson, D. N., Codrescu, M., … Howe, B. M. (2004). Global Assimilation of Ionospheric Measurements (GAIM). *Radio Science*, *39*(1), 1–11. doi: 10.1029/2002rs002794

Seemala, G. K., Yamamoto, M., Saito, A., & Chen, C. H. (2014, apr). Three-dimensional GPS ionospheric tomography over Japan using constrained least squares. *Journal of Geophysical Research: Space Physics*, *119*(4), 3044–3052. doi: 10.1002/2013JA019582

Siefring, C. L., Bernhardt, P. A., James, H. G., & Parris, R. T. (2015). The CERTO Beacon on CASSIOPE/e-POP and Experiments Using High-Power HF Ionospheric Heaters. *Space Science Reviews*, *189*(1-4), 107–122. doi: 10.1007/s11214-014-0110-2

Song, R., Hattori, K., Zhang, X., Liu, J., & Yoshino, C. (2021). Detecting the ionospheric disturbances in Japan using the three-dimensional computerized tomography. *Journal of Geophysical Research: Space Physics*, 1–14. doi: 10.1029/2020ja028561

Song, R., Hattori, K., Zhang, X., & Yoshino, C. (2021). The three-dimensional ionospheric electron density imaging in Japan using the approximate Kalman filter algorithm. *Journal of Atmospheric and Solar-Terrestrial Physics*, *219*(March), 105628. doi: 10.1016/j.jastp.2021.105628

Tamazin, M., Karaim, M., & Noureldin, A. (2018). *Multifunctional Operation and Application of GPS* (R. B. Rustamov & A. M. Hashimov, Eds.). IntechOpen. doi: http://dx.doi.org/10.5772/intechopen.74677

Vierinen, J., Coster, A. J., Rideout, W. C., Erickson, P. J., & Norberg, J. (2016). Statistical framework for estimating GNSS bias. *Atmospheric Measurement Techniques*, *9*(3), 1303–1312. doi: 10.5194/amt-9-1303-2016

Vierinen, J., Norberg, J., Lehtinen, M. S., Amm, O., Roininen, L., Väänänen, A., … McKay-Bukowski, D. (2014). Beacon satellite receiver for ionospheric tomography. *Radio Science*, *49*(12), 1141–1152. doi: 10.1002/2014RS005434

Wang, N., Yuan, Y., Li, Z., Montenbruck, O., & Tan, B. (2016). Determination of differential code biases with multi-GNSS observations. *Journal of Geodesy*, *90*(3), 209–228. doi: 10.1007/s00190-015-0867-4

Yizengaw, E., & Moldwin, M. B. (2005). The altitude extension of the mid-latitude trough and its correlation with plasmapause position. *Geophysical Research Letters*, *32*(9), 1–5. doi: 10.1029/2005GL022854

Zabotin, N. A., Wright, J. W., & Zhbankov, G. A. (2006). NeXtYZ: Three-dimensional electron density inversion for dynasonde ionograms. *Radio Science*, *41*(6), 1–12. doi: 10.1029/2005RS003352